arXiv:1612.04129v1 [cond-mat.mtrl-sci] 13 Dec 2016

Performance of arsenene and antimonene double-gate MOSFETs from first principles

Giovanni Pizzi,[1,*] Marco Gibertini,[1,*] Elias Dib,[2,*] Nicola Marzari,[1] Giuseppe Iannaccone,[2] and Gianluca Fiori[2,†]

[1] *Theory and Simulation of Materials (THEOS) and National Centre for Computational Design and Discovery of Novel Materials (MARVEL), École Polytechnique Fédérale de Lausanne, CH-1015 Lausanne, Switzerland*

[2] *Dipartimento di Ingegneria dell'Informazione, University of Pisa, 56122 Pisa, Italy*

In the race towards high-performance ultra-scaled devices, two-dimensional materials offer an alternative paradigm thanks to their atomic thickness suppressing short-channel effects. It is thus urgent to study the most promising candidates in realistic configurations, and here we present detailed multiscale simulations of field-effect transistors based on arsenene and antimonene monolayers as channels. The accuracy of first-principles approaches in describing electronic properties is combined with the efficiency of tight-binding Hamiltonians based on maximally-localised Wannier functions to compute the transport properties of the devices. These simulations provide for the first time estimates on the upper limits for the electron and hole mobilities in the Takagi's approximation, including spin-orbit and multi-valley effects, and demonstrate that ultra-scaled devices in the sub-10 nm scale show a performance that is compliant with industry requirements.

Introduction

In the past decades the exponential increase in computing power predicted by Moore's law has been enabled by scaling complementary metal-oxide-semiconductor (CMOS) silicon-based devices, i.e., reducing their size and limiting at the same time their power dissipation, while increasing the operating frequency. With transistor dimensions going below 10 nm, fundamental limitations are emerging both in terms of manufacturing costs and device performance. To sustain Moore's law, a paradigm shift either in device architecture or in materials is needed.

In this respect, using 2D systems as conduction channels is definitely one of the most exciting opportunities[1]. Indeed, their ultimate thinness can reduce short-channel effects, one of the main detrimental factors for devices at ultrashort lengths. For this reason, starting with the experimental realisation of graphene[2], single-layer materials have gained considerable attention for a large number of different applications. Several studies, in particular, have targeted graphene as a component of novel devices, motivated by its exciting electronic, mechanical and thermal properties, such as its extremely high mobility [3]. Despite its appeal, graphene has regrettably no gap. Therefore, it is not suited for electronic applications such as field-effect transistors (FETs), where a semiconductor material with a finite gap is required for device switching. The first suitable candidate, the transition-metal dichalcogenide (TMDC) MoS_2,[4] has been shown to be an interesting transistor material, even if its mobility is much lower than that of graphene[5]. The list of relevant two-dimensional systems has then been enriched by other TMDCs [6] and by many other layered materials, such as black phosphorus and its monolayer form phosphorene, that is promising for its high mobility[7–12].

In light of the current pace at which 2D materials are being identified, we cannot expect that each new candidate is grown experimentally with high quality and then devices with various geometries are fabricated, characterised and optimised. Instead, simulations can be used to efficiently determine and optimise materials properties and device characteristics and filter only a few systems to send then to the laboratory. Promising candidates can be considered, for instance, by looking for materials chemically similar to existing ones. As an example, two new monolayer materials composed of group–V elements (in analogy with phosphorene) have been recently theoretically investigated: arsenene and antimonene,[13–16] made of As and Sb, respectively. The authors have put forward the hypothesis that they could be attractive for device applications. While this suggestion is reasonable, only an accurate simulation of a complete device can support this hypothesis and will further stimulate experimental interest[17] in these novel 2D materials.

This task is not straightforward, however, because the simulation of a device requires a preliminary characterisation of the material. While properties and parameters are available in the literature for well-studied systems (such as bulk Si or III-V semiconductors), in the case of new materials they are typically not available, nor they can be easily extracted from known systems; they must instead be calculated from first principles. This can be true even in simple cases: for instance, despite their chemical similarity, arsenene and antimonene display very different electronic and mechanical properties with respect to phosphorene, as they originate from different allotropes and have thus a completely different crystal structure. On the other hand, performing a full device simulation directly from first principles is compu-

* These authors contributed equally to this work
† gfiori@mercurio.iet.unipi.it

tationally out of reach. Device simulators based on effective tight-binding Hamiltonians [18, 19] are viable, but require the knowledge of on-site and hopping energies, and a few different methods have been proposed in the literature to address the issue of bridging the different simulation scales [20, 21].

Here, we adopt a multiscale approach based on maximally localised Wannier functions (MLWF) [22], while providing a physical understanding of the transport properties of monolayer As and Sb. Basic electronic properties are calculated from first principles using density-functional theory (DFT). The electronic wavefunctions are then used as input to obtain MLWF in a multiscale approach, providing us with an effective tight-binding Hamiltonian for the relevant electronic bands around the fundamental gap, and retaining at the same time full first-principles accuracy in the results.[23, 24] MLWF are used to characterise the material (e.g., effective masses) by exploiting the efficient band interpolation, and as a localised tight-binding basis set to simulate the currents in a complete device with a non-equilibrium Green function (NEGF) formalism [25]. In particular, we consider double-gate metal-oxide-semiconductor field-effect transistors (MOSFETs) based on arsenene and antimonene channels and compare their performance against Industry requirements. We show that such devices have the potential to achieve the target set by the International Technology Roadmap for Semiconductors (ITRS) [26] for future competitive devices for high performance digital applications, in particular in terms of the capability of behaving as an outstanding switch even in the ultra-scaled regime.

Results

Multiscale material characterisation

The first step towards the multiscale simulation of devices based on As and Sb monolayers is the computation from first principles of their electronic structure. To perform this task, we carried out DFT simulations using the Quantum ESPRESSO[27] suite of codes, efficiently automated using AiiDA[28] (more details in the Methods section). All calculations reported here include spin-orbit coupling (SOC) effects. In the Supplementary Note 1 we discuss in detail the effect of SOC and compare the results obtained here with those without SOC.

In Fig. 1a we show the equilibrium crystal structure of arsenene and antimonene. Differently to phosphorene, As and Sb monolayers are not puckered, but display a buckled structure more similar to silicene or germanene [29, 30], with two inequivalent atoms inside the primitive hexagonal unit cell lying on two different planes. (Note that As and Sb have also been predicted to exist in a puckered structure, but this phase is energetically less favourable [13, 14]). The separation d between the planes reads 1.394 Å for As and 1.640 Å for Sb, while the equilibrium lattice constant a is, respectively, 3.601 Å and 4.122 Å. The band structure of both materials is very similar and in Fig. 1b we show the energy bands along a high-symmetry path in the Brillouin zone obtained from DFT (empty circles) in the case of arsenene (for the bands of antimonene see Supplementary Figure 1). The DFT band gap is indirect (for both materials) and equal to 1.48 eV for As and 1.00 eV for Sb. The maximum of the valence bands is located at the Γ point and, without SOC, it would be two-fold degenerate; the inclusion of the SOC splits the degeneracy (see Fig. 1b and Supplementary Figure 2) and the topmost valence band becomes non-degenerate, except for the twofold spin degeneracy. The minimum of the conduction bands lies instead along the $\Gamma-$M line and gives rise to six valleys.

Further analyses of the electronic properties of arsenene and antimonene have been performed by first mapping the Bloch eigenstates associated with the bands around the gap into a set of maximally localised Wannier functions[22]. We focused in particular on the three top valence bands and three bottom conduction bands (per spin component). The main orbital contribution to these bands comes from p-orbitals of the atoms that form bonding and antibonding combinations around the gap. By projecting over the p-orbitals of the two atoms in the primitive cell, the standard localisation procedure leads to six Wannier functions per spin component, three centred on one atom and three on the other. In Fig. 1a we show the spatial profile of the three Wannier functions centred on atoms belonging to the lower plane (the other three can be obtained simply by spatial inversion through a mid-bond centre). They clearly have a p-like character with minor contributions from neighbouring atoms. From the knowledge of these Wannier functions it is straightforward to compute the matrix elements of the Hamiltonian between them.

In such a way, it becomes possible to interpolate efficiently the Hamiltonian at any arbitrary $\mathbf{k}-$point in reciprocal space, keeping the same accuracy of the underlying first-principles simulation, but at an extremely reduced computational cost. In Fig. 1b we show the Wannier-interpolated energy bands (red solid lines) with a much denser mesh than the original DFT results (empty circles) for As monolayer (bands for Sb monolayer are shown in Supplementary Figure 1). Exploiting such interpolation scheme, we also computed the effective masses for relevant band extrema that crucially affect carrier mobilities and intraband tunnelling amplitudes. We both fitted the electronic bands along principal directions and evaluated accurately the density-of-states (DOS) on an extremely dense grid. The values of the masses are reported in Table 1 for both materials. In particular, for the valence band maxima, the SOC splits

the degeneracy of the two topmost bands at Γ. Since the magnitude of the splitting is large, for realistic band filling levels we can limit ourselves to consider only the topmost valence band, with (isotropic) mass $m^{\rm v}$. (If SOC was neglected, we would need instead to consider both degenerate bands, as discussed in Supplementary Notes 2–5 and Supplementary Figures 2–5.) For the conduction bands, the isoenergies of the six valleys are oblate with a larger effective mass $m^{\rm c}_{\rm L}$ in the longitudinal direction with respect to the transverse effective mass $m^{\rm c}_{\rm T}$. The effective DOS mass for each valley $m^{\rm c}_{\rm DOS}$ computed independently is in agreement with what can be expected from geometrical arguments, i.e. $m^{\rm c}_{\rm DOS} \approx \sqrt{m^{\rm c}_{\rm L} m^{\rm c}_{\rm T}}$.

As a first assessment of the material properties toward the realisation of a transistor device using arsenene or antimonene as channel materials, we estimate whether the ballistic approximation is valid at room-temperature ($T = 300\,{\rm K}$) in the ultrascaled sub-10 nm regime that we investigate in this work. We will limit the analysis only to the intrinsic scattering with longitudinal acoustic (LA) phonons. As other scattering mechanisms may be active in the system, the values that we calculate should be considered as upper limits to the actual scattering times or, equivalently, to the carrier mobility. In particular, while out-of-plane (ZA) phonons may play an important role in free-standing Dirac materials without planar symmetry [31, 32], we do not consider them here. While in a free-standing material scattering with ZA phonons can be relevant, in our systems the device geometry (presence of substrate and of top gates) will shift the ZA phonon modes at finite energy, reducing their impact on the mobilities.[33]

While accurate values for the electron-phonon scattering terms can be obtained fully ab-initio [34, 35], an efficient method to get estimates for the scattering times and mobilities relies on deformation-potential theory[36] and Fermi's golden rule to estimate the scattering times. An estimate of the 2D mobility can be then obtained using Takagi's formula [9, 37, 38]

$$\mu_{\rm 2D} = \frac{e\hbar^3 C_{\rm 2D}}{k_{\rm B} T m^*_{\rm e} m_{\rm DOS} (E^i)^2}, \qquad (1)$$

where $m^*_{\rm e}$ is the transport effective mass, $m_{\rm DOS}$ the DOS effective mass (Table 1), $k_{\rm B}$ the Boltzmann constant, T the temperature, E^i the deformation potential constant, and $C_{\rm 2D}$ the elastic modulus. In our case, we need to consider this formula in the multi-valley, anisotropic case: details can be found in Supplementary Notes 3–9 and described in Supplementary Figures 3–7, as well as the values of the extracted relevant parameters (deformation potentials and elastic moduli, reported in Supplementary Tables 1 and 2, respectively).

We would like to emphasise, however, that this formula, while often adopted in the literature, cannot be used to obtain a quantitative estimate of the mobility. Indeed, the formula neglects the coupling with ZA phonons (which may be important, as already discussed above), as well as with TA and optical phonons. Moreover, it cannot fully capture the anisotropy of the electron-phonon coupling coefficients. A full ab-initio treatment of the electron-phonon scattering is required, if a quantitative estimation is needed (see e.g. discussions in Refs. 31 and 39). Nevertheless, we provide here an estimate of what we will call hereafter Takagi's mobilities, mainly to allow to compare As and Sb with other 2D materials already investigated in the literature within the same level of theory. We have estimated that, in the worst case scenario, the values of actual mobilities could be reduced up to a factor of 8 when a full treatment of the electron-phonon coupling is adopted, including intervalley scattering.

The resulting values of the electron Takagi's mobility $\mu_{\rm c}$ and the hole Takagi's mobility $\mu_{\rm h}$ are 635 and 1700 $\rm cm^2V^{-1}s^{-1}$, respectively, for As and 630 and 1737 $\rm cm^2V^{-1}s^{-1}$ for Sb.

The values of the electron Takagi's mobility are quite promising and comparable with theoretical results for phosphorene using the same level of theory[9] and even better than MoS_2[40] owing to the smaller deformation potential. The hole Takagi's mobility is even larger, and in particular much larger than the experimentally measured value of the mobility in MoS_2 at room temperature[41] and in other 2D materials, like e.g. phosphorene[8]. On the other hand, we note that our predicted values are smaller than those predicted by simulations at the same level of theory (Takagi's formula) for phosphorene[9], owing to the larger elastic modulus and smaller deformation potential in the zigzag direction.

We also emphasise that in arsenene and antimonene the SOC effects are negligible for the conduction band. Instead, $\mu_{\rm h}$ is significantly enhanced by the SOC, due to the splitting of the topmost valence band and the resulting changes in the effective masses and deformation potentials (see Supplementary Tables 1 to 3). In particular, the inclusion of the SOC increases $\mu_{\rm h}$ by 25% and 84% in As and Sb, respectively (see Supplementary Table 4).

From these values of the Takagi's mobilities and the associated scattering times and carrier velocities reported in the Supplementary Note 10, we estimate that the mean free path limited by LA phonons is of the order of tens of nm. For this reason we assume that, for the dimensions considered in this work, the use of the ballistic approximation is justified and sets a higher limit to the performance achievable in these devices.

Performance of arsenene and antimonene based devices

In view of the results of the previous section, we perform a full device simulation of field-effect transistors based on arsenene and antimonene as channel materi-

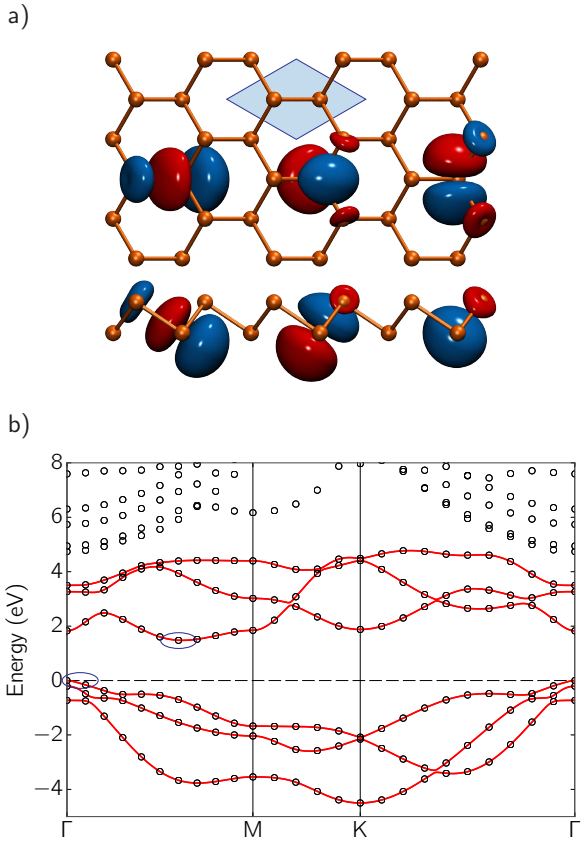

FIG. 1. **Structure, energy bands, and Wannier functions of As and Sb monolayers:** (a) Top and lateral views of As or Sb monolayers. The blue shaded region represents the primitive unit cell comprising two inequivalent atoms. The spatial profile of three maximally-localised Wannier functions is also reported. Isosurfaces of different colours (red and blue) correspond to opposite values of the real-valued Wannier functions. (b) Energy bands of arsenene along a high-symmetry path in the Brillouin zone. Empty circles denote the results of a direct DFT calculation while red solid lines represent the Wannier-interpolated bands. Blue circles highlight the position of the valence band maximum and conduction band minimum.

als; we will focus in particular on n-type devices since, as shown in Supplementary Note 10, they show better performance as compared to p-type FETs. Our aim is to assess quantitatively whether such devices can comply with industry requirements for high-performance applications as needed by the ITRS [26], which sets electrical and geometrical device parameters to keep the pace with Moore's Law [42]. The simulated device structure is shown in Fig. 2. We consider a double-gate transistor with doped source and drain, SiO_2 as gate dielectric, and gate lengths ranging from 5 to 7 nm. The supply voltage (V_{DD}) and the oxide thickness (t_{ox}) are chosen according to the device channel length (L_G), as specified by ITRS. Spin-orbit coupling has been taken into account.

TABLE 1. **Valence and conduction effective masses of arsenene and antimonene:** Effective masses of the relevant bands of arsenene and antimonene, in units of the electron mass m_0, when SOC effects are included. Symbols are explained in the main text. Note that m^c_{DOS} is the effective DOS mass for each of the 6 identical conduction band valleys.

	As	Sb
m^c_{DOS}	0.270	0.261
m^c_L	0.501	0.472
m^c_T	0.146	0.144
m^v	0.128	0.103

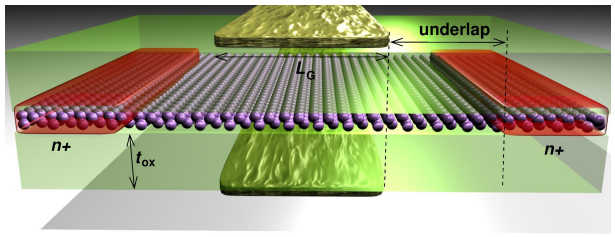

FIG. 2. **Double-gate n-doped MOSFETs:** Schematic view of the double-gate n-doped MOSFETs studied here, where the channel is either an As or an Sb monolayer. In the figure, the doped contacts, the gate and the oxide are shown, together with the main geometrical parameters of the device.

Figure 3 shows the transfer characteristics of As- and Sb-based MOSFETs for the set of parameters listed in Table 2. For a fair comparison, the gate work function of all devices has been shifted in order to have the same off-current $I_{OFF} = 0.1$ A m^{-1} at $V_{GS} = V_{OFF} = 0$ V, i.e., the smallest current driven by the transistor. Both As and Sb transistors show similar $I-V$ characteristics as a consequence of their very similar conduction bands [15].

From the $I-V$ characteristics, we can extract the main figures of merit (FOM) required to assess the device performance, that we summarise in Table 2. In particular, the subthreshold swing (SS), defined as the inverse slope of the $I_{DS} - V_{GS}$ curve in semi-logarithmic scale in the subthreshold regime, provides relevant information regarding the sensitiveness of the device to short-channel effects: the smallest SS achievable in thermionic devices at room temperature is equal to 60 mV dec^{-1}. [43] For a gate length of 7 nm, both As and Sb based MOSFETs exhibit excellent SS: 64 mV dec^{-1} and 60 mV dec^{-1}, respectively. As the channel length gets shorter (L_G = 6 and 5 nm), SS increases to 81 mV dec^{-1} and 106 mV dec^{-1} for As, and 83 mV dec^{-1} and 106 mV dec^{-1} for Sb transistors, respectively. The reported values of SS for both materials show very promising performances, maintaining a subthreshold slope of approximately 100 mV dec^{-1} even for the smallest devices.

Another FOM is the I_{ON}, i.e., the largest current driven by the transistor (for V_{GS}=V_{DS}=V_{DD}.) All our

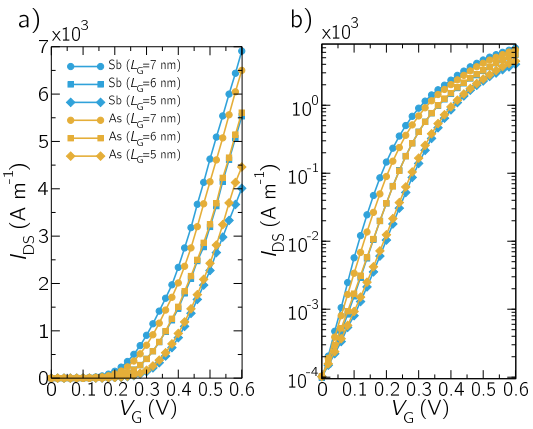

FIG. 3. **Transfer characteristics of As- and Sb-based MOSFETs:** $I_{\rm DS} - V_{\rm GS}$ curve in (a) linear and (b) semi-logarithmic scale for Sb (light-blue lines) and As (yellow lines) transistors with $L_{\rm G} = 7$ nm, $V_{\rm DS} = 0.6$ V and $t_{\rm ox} = 0.5$ nm (circles), $L_{\rm G} = 6$ nm, $V_{\rm DS} = 0.57$ V and $t_{\rm ox} = 0.45$ nm (squares) and $L_{\rm G} = 5$ nm, $V_{\rm DS} = 0.54$ V and $t_{\rm ox} = 0.42$ nm (diamonds).

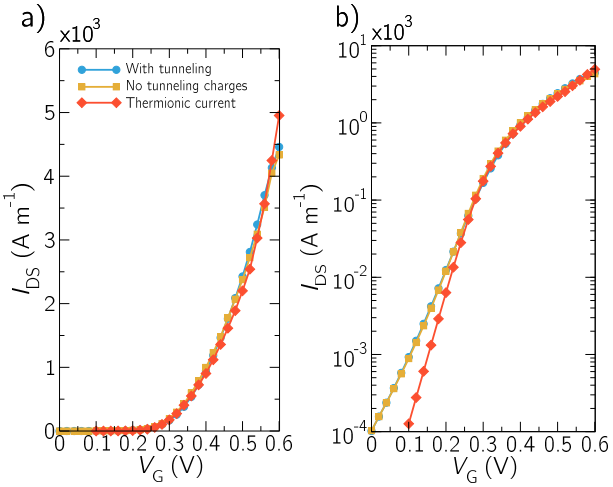

FIG. 4. **Short-channel effects on sub-threshold swing:** $I_{\rm DS} - V_{\rm GS}$ curve in (a) linear and (b) semi-logarithmic scale for As transistors with $L_G = 5$ nm and $V_{\rm DS} = 0.54$ V. The full simulation model considering tunnelling both in the current and the charges is represented by light-blue circles, whereas suppressed charges in the channel and thermionic currents only are represented by yellow squares and red diamonds, respectively.

considered devices comply with $I_{\rm ON}$ requirements from ITRS. It is important to say that in our calculation the contact resistance has been neglected, and therefore our results represent an upper limit for the achievable $I_{\rm ON}$.

The intrinsic delay time τ and the dynamic power indicator (DPI) provide instead information regarding the switching speed and the power consumption of a device, respectively. The values we obtain comply with ITRS requirements, even for the shortest gate length. In particular, DPI and τ are the energy and the time it takes to switch a CMOS NOT port from the logic 1 to the logic 0 and viceversa, respectively. In the same Table 2, we also show the cut-off frequency $f_{\rm T}$, i.e., the frequency for which the current gain of the transistor is equal to one, which is a relevant parameter for radio-frequency applications. Both As and Sb MOSFETs exhibit excellent $f_{\rm T}$ compared to ITRS. As compared to other two-dimensional materials, As and Sb show performance comparable to that obtained in black phosphorus FETs [44, 45].

To get a deeper understanding of the effects limiting the device performance, we focus in particular on the degraded subthreshold swing observed in short-channel devices, which can be attributed to two main phenomena: large tunnelling currents through the narrow barrier; and large parasitic capacitance at source/drain-channel junctions, i.e., short channel effects. To elucidate which of the two effects plays a major role, we consider them separately for the shortest device: we either neglect quantum phenomena for the current (i.e., tunnelling through the channel barrier), but not when computing the charge (i.e., we consider mid-gap tunnelling states when solving the electrostatic problem, red line in Fig. 4) or viceversa (yellow line in Fig. 4). Transfer characteristics with almost ideal SS (~ 60 mV dec^{-1}) are obtained in the first case, demonstrating that the SS in short-channel devices is limited by the fact that the channel barrier is almost transparent for electrons injected from the source reservoir, and not by the short-channel effects, as one may expect for such short channel lengths. This suggests that, from an engineering point of view, in order to improve the performance in ultra-scaled devices, efforts have to be directed in increasing the opacity of the channel barrier. This can be achieved for example exploiting materials with larger longitudinal tunnelling effective masses, or using uniaxial strain to split the conduction valleys while selecting bands with larger tunnelling effective mass in the transport direction.

Performing an investigation along the device parameter space, we have also computed the $I - V$ characteristics for different gate underlap values (defined in Fig. 2), fixing the distance between source and drain electrodes (i.e., 7 nm) and changing accordingly the gate length $L_{\rm G}$ and the underlap region, and the source and drain doping concentrations (Fig. 5 and Fig. 6, respectively). As it can be seen from the results reported in Fig. 5, $I - V$ curves change only marginally when considering different underlap values. As a consequence, from a fabrication point of view, while control of the geometrical parameters for the gate contacts is required, minor dispersions do not drastically degrade the device performance. From Fig. 6, instead, we deduce that the sub-threshold slope improves

TABLE 2. **Performance of arsenene and antimonene n-MOSFETs:** Device parameters and calculated figures of merit of As- and Sb-based n-MOSFETs for different channel lengths. The target FOMs set by ITRS for end-of-the-roadmap are also indicated [26]. The meaning of each parameter is explained in the main text.

		As			Sb		
L_G (nm)		7	6	5	7	6	5
t_{ox} (nm)		0.5	0.45	0.42	0.5	0.45	0.42
V_{DD} (V)		0.6	0.57	0.54	0.6	0.57	0.54
SS (mV dec^{-1})	[this work]	64	81	106	60	83	106
I_{ON} (A m^{-1})	[ITRS]	$\geq 2.19 \times 10^3$	$\geq 2.31 \times 10^3$	$\geq 2.41 \times 10^3$	$\geq 2.19 \times 10^3$	$\geq 2.31 \times 10^3$	$\geq 2.41 \times 10^3$
	[this work]	6.57×10^3	4.9×10^3	3.2×10^3	6.91×10^3	4.93×10^3	2.98×10^3
τ (ps)	[ITRS]	≤ 0.125	≤ 0.1	≤ 0.08	≤ 0.125	≤ 0.1	≤ 0.08
	[this work]	0.04	0.045	0.052	0.042	0.047	0.055
f_T (THz)	[ITRS]	≥ 1.91	≥ 2.36	≥ 2.88	≥ 1.91	≥ 2.36	≥ 2.88
	[this work]	5.8	6.01	5.47	5.51	5.94	4.83
DPI (10^{-10} J m^{-1})	[ITRS]	≤ 1.6	≤ 1.4	≤ 1.2	≤ 1.6	≤ 1.4	≤ 1.2
	[this work]	1.58	1.25	0.91	1.76	1.31	0.89

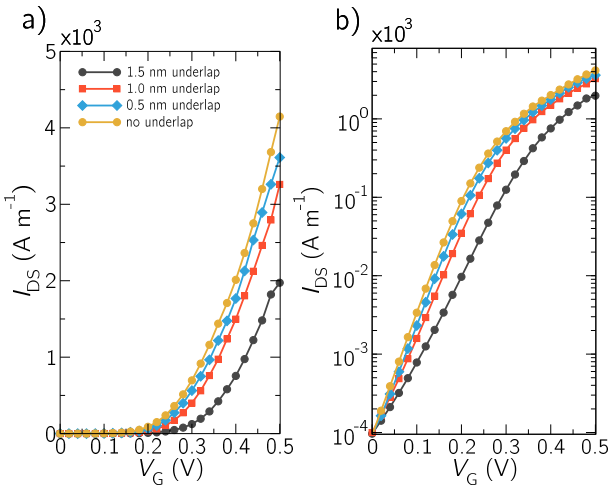

FIG. 5. **Transfer characteristics for different underlap:** $I_{DS}-V_{GS}$ curve in (a) linear and (b) semi-logarithmic scale for As transistors with total distance between drain and source electrodes of 7 nm, and different underlap.

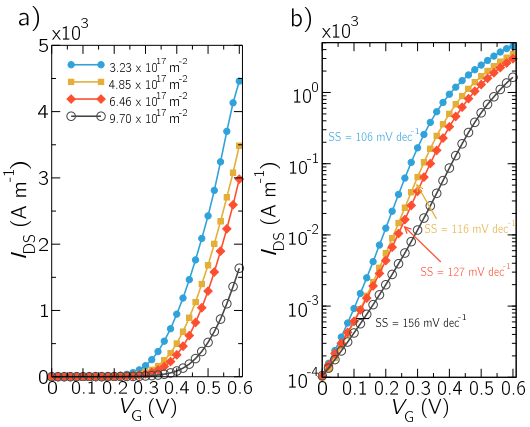

FIG. 6. **Boosting device performances by tuning source and drain doping concentrations:** $I_{DS}-V_{GS}$ curve in (a) linear and (b) semi-logarithmic scale for As transistors with $L_G = 5$ nm and for different source and drain doping concentrations.

significantly when the doping is reduced. Therefore, the doping concentration can be used as an additional parameter to optimise the device performance.

Discussion

In summary, we have provided a comprehensive analysis of 2D FET transistors based on arsenene and antimonene (i.e., monolayers composed of As and Sb, respectively), demonstrating that these materials are promising for high-performance devices for digital applications. Our single-valley and multi-valley upper estimates of the mobilities in the Takagi's approximation show that high phonon-limited mobilities can potentially be obtained both in monolayer As and Sb, even if ab-initio simulations of the electron-phonon scattering are required to obtain quantitative predictions for this quantity. This result motivated our extensive investigation of device performance using a multiscale approach, where the predictive power of density-functional-theory calculations has been incorporated into an efficient tight-binding model using maximally-localised Wannier functions. When exploited as channel materials in field-effect transistors, arsenene and antimonene show a performance compliant with industry requirements for ultra-scaled channel lengths below 10 nm, where the ultimate atomic thickness of the exploited 2D materials effectively manages to suppress short-channel effects and tunnelling starts to play a major role. We expect therefore that our predictions will provide a strong motivation for further experimental investigation of these novel materials.

Methods

First-principles calculations – All first-principles calculations have been performed using density-functional theory (DFT) as implemented in the pw.x code of the Quantum ESPRESSO v.5.1.2 distribution [27], using the PBE exchange–correlation functional [46]. Pseudopotentials and energy cutoffs in a plane-wave basis have been chosen using the converged results provided in the SSSP pseudopotential library [47] for calculations without SOC. In particular, we used an ultrasoft pseudopotential [48] from PSLibrary [49] with cutoffs of 40 and 320 Ry (for the expansion of the wavefunctions and the charge density, respectively) for As; and an ultrasoft pseudopotential from the GBRV library [50] (with cutoffs of 50 and 400 Ry, respectively) for Sb. For calculations including SOC we used instead norm-conserving pseudopotentials from the Pseudo Dojo project [51] with cutoffs of 40 and 160 Ry (for the expansion of the wavefunctions and the charge density, respectively) for As; and with cutoffs of 80 and 320 Ry, respectively, for Sb. Supercells with 20 Å of vacuum in the direction orthogonal to the layers have been considered to minimise the interaction between periodic replicas. Integrals on the Brillouin zone have been performed on a $14 \times 14 \times 1$ $\Gamma-$centred grid for the primitive cell (two atoms) and on a $6 \times 10 \times 1$ $\Gamma-$centred grid for the rectangular supercell (containing four atoms). Convergence on the charge density in the self-consistent loop was considered achieved when the estimated energy error was smaller than 1×10^{-8} meV. Structures have been relaxed using the Broyden–Fletcher–Goldfarb–Shanno algorithm until forces were smaller than 1 meV Å^{-1}. The same parameters have been used also for relaxing atomic positions at fixed cell for the evaluation of elastic moduli and deformation potentials.

Wannier functions – MLWF [22, 52, 53] have been computed using v.2.1 of the Wannier90 code [54, 55]. The same k-grids used for the computation of the DFT charge densities have been employed to compute the wavefunctions and overlap matrices used as input to calculate Wannier functions. The lower-energy bands have been explicitly excluded from the calculation: with the pseudopotentials we used, 2 for As and 12 for Sb in the primitive cell (4 and 24, respectively, when considering explicitly the spin degeneracy), and only 6 bands (12 with spin degeneracy) around the fundamental gap have been considered. We have chosen p-type orbitals centred on each atom in the cell as initial projections. Convergence has been considered achieved when the change in the total spread was smaller than 10^{-12} Å^2 for at least 20 iterations. Wannier functions have then been used to compute band structures and density of states on denser $\mathbf{k}-$grids (400×700 in the rectangular cell). DFT and Wannier calculations have been managed using the AiiDA framework[28] v. 0.5.0 to manage, automate and store in a graph database calculations, results, and computational workflows (e.g., for band structure calculations, Wannierisation, effective mass evaluations).

Device simulations – The Hamiltonian expressed on the MLWF basis set has been exploited in order to compute transport within the NEGF formalism [25]. The system is considered infinite along the zigzag direction (with Bloch periodic boundary conditions), while the transport channel is along the armchair direction. To compute the currents in the device in the ballistic regime, we have used the open-source NanoTCAD ViDES [18] code. In particular, in order to accurately reproduce the energy bands obtained from first-principles, up to 58 nearest-neighbours have been included in the Hamiltonian, and transport problems have been solved considering 30 wavevectors in the Brillouin zone and an energy step of 1 meV. For the electrostatic problem, the two-dimensional Poisson equation has been solved, while potential translational invariance has been considered in the direction transversal to transport. All transport calculations are performed at room temperature. In all device simulations (except where explicitly otherwise mentioned) a doping concentration of 3.23×10^{17} m^{-2} has been considered for the source and drain contacts.

Acknowledgements

We thank Nicolas Mounet for providing us with the AiiDA workflow to compute band structures with Quantum ESPRESSO and Massimo Fischetti for very insightful discussions. This work was supported by a grant from the Swiss National Supercomputing Centre (CSCS) under project IDs s580. M.G., N.M., G.I. and G.F. gratefully acknowledge the Graphene Flagship (contract 604391).

Supplementary Information

Supplementary Note 1: Band structure of antimonene, and spin-orbit coupling effects

In the paper, only the band structure of arsenene has been shown, because the band structure of antimonene is qualitatively the same. For completeness we report in this Supplementary Information, in Supplementary Figure 1, the band structure of antimonene as well as the bands interpolated using maximally-localised Wannier functions. Moreover, we compare all results with the case in which the spin-orbit coupling (SOC) has been set to zero, showing that the SOC almost does not change the final results for the mobilities in the conduction band, while it significantly affects results in the valence (due to the splitting of the degeneracies). In particular, in Supplementary Figure 2 we compare the

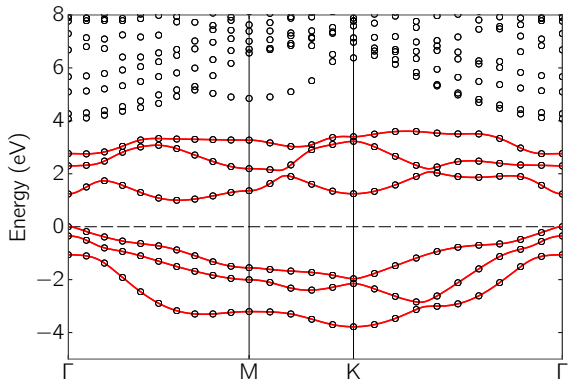

Supplementary Figure 1. Energy bands of antimonene along a high-symmetry path in the Brillouin zone, including spin-orbit coupling effects. Empty circles denote the results of a direct DFT calculation while red solid lines represent the Wannier-interpolated bands. The zero of energy is set to the top of the valence bands.

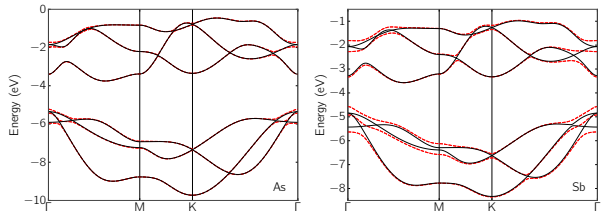

Supplementary Figure 2. Wannier-interpolated energy bands of arsenene (left panel) and antimonene (right panel) along a high-symmetry path in the Brillouin zone, comparing the band structure calculated including (red dashed lines) and disregarding (solid black lines) spin-orbit coupling effects. The bandgaps without SOC are 1.62 eV and 1.29 eV for As and Sb, respectively, while the valence-band splitting due to the SOC is 0.208 eV and 0.349 eV, respectively. The values of the bandgaps with SOC are reported in the main text. The zero of energy is set at the vacuum level.

(Wannier-interpolated) band structures of As and Sb, to show the effect of the spin-orbit coupling on the electronic bands.

Supplementary Note 2: Calculation of mobilities

We describe in detail in this Section how we calculated the phonon-limited mobilities of the 2D systems considered in the paper.

We calculate mobilities using the Boltzmann transport equation, where the relaxation time for scattering with LA phonons is computed using deformation potential theory [36] in the effective mass approximation. For a single-valley, non-degenerate band, the reciprocal of the scattering time with LA phonons propagating in the β direction for the $i-$th band at $\mathbf{k}-$point $\mathbf{k}$ is given by [36, 38]:

$$\frac{1}{\tau_\beta(i,\mathbf{k})} = \frac{2\pi k_\mathrm{B} T (E^i_\beta)^2}{\hbar C_\beta} \sum_{\mathbf{k}'} \delta\left[\varepsilon_i(\mathbf{k}) - \varepsilon_i(\mathbf{k}')\right](1-\cos\theta), \tag{S1}$$

where k_B is the Boltzmann constant, E^i_β is the deformation potential of the $i-$th band for deformations in the β direction, C_β is the 2D elastic modulus for strains along β, $\varepsilon_i(\mathbf{k})$ is the energy of the $i-$th band at $\mathbf{k}$, and we are replacing for simplicity the scattering angle weighting factor with $(1-\cos\theta)$ (valid for a spherical energy surface, where θ is the angle between $\mathbf{k}$ and $\mathbf{k}'$).

The calculation of the various coefficients is described in the next sections. To get the value of the mobility, though, it is easier to work out the formula in the specific case of a 2D system. By replacing the sum over $\mathbf{k}'$ with an integral, and then passing from an integral over the Brillouin Zone to an integral over energies, we obtain that

$$\frac{1}{\tau_\beta} = \frac{k_\mathrm{B} T (E^i_\beta)^2 (m^*_\mathrm{DOS})_i}{\hbar^3 C_\beta}. \tag{S2}$$

Finally, the mobility μ is diagonal relative to the axes of the effective mass of the valley of interest [56], and its diagonal components can be obtained as

$$\mu_{\beta\beta} = e\,\langle\tau_\beta\rangle \cdot \left(\frac{1}{m^*}\right)_{\beta\beta} \tag{S3}$$

with e being the electron charge, $(1/m^*)$ the inverse effective mass tensor, and $\langle\tau\rangle$ the average scattering time (as defined in Eq. (16) of Ref. [56]). The formula is valid in the same reference frame in which the effective mass tensor is diagonal. Note that in the 2D case, $\langle\tau\rangle = \tau$ since there is no energy dependence.

In the case of multiple valleys or degenerate bands, the expression for the mobility is the same of Supplementary Equation (S3), but applies to a single valley. To understand how the mobilities need to be added, it is easier to write them in terms of the electrical conductivity σ, using the fact that the total conductivity is the sum of the conductivities of the different channels. To do so, we notice that we can write the mobility μ^i of Supplementary Equation (S3) as

$$\mu^i = \frac{\sigma^i}{n^i e}, \tag{S4}$$

for each valley i contributing to the transport, where n^i is the charge in the $i-$th valley. Using $\sigma_\mathrm{T} = \sum_i \sigma^i$, where σ_T represents the total conductivity, we obtain therefore for the total mobility:

$$\mu_\mathrm{T} = \frac{\sum_i \mu^i n^i}{\sum_i n^i}. \tag{S5}$$

Supplementary Note 3: Relevant band edges: generic discussion

As already discussed in the paper, the bands of As and Sb are quite similar, so the following discussion applies to both systems, unless explicitly mentioned.

As it is visible from the band structure of the two materials (see Supplementary Figure 1, and Figure 1 in the main paper), the relevant band edge to consider in the conduction is the minimum along the Γ−M line. All other conduction band edges (for instance, the minimum at Γ or at the K point) are several hundreds of meV above the one along Γ−M, and therefore do not contribute to transport at room temperature for typical doping levels. We have also verified that this condition holds at least for a strain range between −1 and 1%. In the unstrained case, this minimum is composed of six degenerate valleys, along the six equivalent Γ−M lines. In the rectangular supercell shown in blue in Supplementary Figure 3(a), two of these lines fold along the Γ−X line, while four fold on the Γ−S lines, as shown in Supplementary Figure 3. When a uniaxial strain is applied, the degeneracy is lost and the six valleys split in two groups (the two Γ−X and the four Γ−S valleys), with different deformation potentials. We also stress that in the rectangular cell, the Γ−S line is not anymore a high-symmetry line, so the band edge can also move out of this line. Note that, actually, for the evaluation of the mobility we just need the deformation potential along the two principal axes of the effective mass, that is, we just need the values for the Γ−X lines, both for strains along the armchair and zigzag directions. This discussion holds both with and without SOC.

In the valence, in the case without SOC, the only relevant band edges are the two degenerate maxima at Γ (also in this case other local maxima are further down in energy and can be disregarded for the calculation of the mobility). These are both single-valley maxima, but they split when a uniaxial strain is applied because they have different deformation potentials. When including SOC effects, the degeneracy is split and, for realistic band filling levels ($\lesssim 10^{13}$ cm^{-2}), we can limit our calculations only to the topmost valence band, since it is the only ones going to be filled.

Let us now compute an explicit formula for the mobilities for the As and Sb monolayer systems:

Supplementary Note 4: Relevant conduction band edges

The mass tensor of each of the 6 Γ−M valleys is non-isotropic, with a longitudinal mass $m_{\rm L}^{\rm c}$ along the Γ−M direction, and a transverse mass $m_{\rm T}^{\rm c}$ in the orthogonal direction. The inverse-mass tensor in a basis set where the first vector is along the longitudinal direction is therefore:

$$\left(\frac{1}{m^*}\right)_{ij} = \begin{pmatrix} \frac{1}{m_{\rm L}^{\rm c}} & 0 \\ 0 & \frac{1}{m_{\rm T}^{\rm c}} \end{pmatrix}. \tag{S6}$$

In this basis set, the two τ_β to calculate are along the longitudinal direction (corresponding to strains along the armchair direction, see Supplementary Figure 3), and along the transverse direction (zigzag). Therefore, substituting Supplementary Equation (S2) into Supplementary Equation (S3), the mobility tensor for a single valley, in this basis set, will be:

$$\boxed{\mu^{{\rm cond},i} = \frac{e\hbar^3}{k_{\rm B}T m_{\rm DOS}^{\rm c}} \begin{pmatrix} \frac{C_{\rm armchair}}{(E_{\rm armchair}^{\rm cond})^2 m_{\rm L}^{\rm c}} & 0 \\ 0 & \frac{C_{\rm zigzag}}{(E_{\rm zigzag}^{\rm cond})^2 m_{\rm T}^{\rm c}} \end{pmatrix},} \tag{S7}$$

with $m_{\rm DOS}^{\rm c}$ being the DOS mass of a single conduction valley.

Since the DOS effective mass is the same for each valley and the valleys are degenerate (in the absence of strain that splits the bands, as discussed above), all valleys have the same population $n^i = n/6$ and therefore the total conductivity is simply:

$$\mu_{\rm T}^{\rm cond} = \frac{1}{6}\sum_{i=0}^{5} \mu^{{\rm cond},i}, \tag{S8}$$

where the tensors $\mu^{{\rm cond},i}$ must, however, be rotated. We remind here that given a tensor $\begin{pmatrix} \alpha & 0 \\ 0 & \beta \end{pmatrix}$ in a reference frame in which it is diagonal, its form in a frame rotated counterclockwise by an angle θ is

$$\begin{pmatrix} \alpha\cos^2\theta + \beta\sin^2\theta & (\beta-\alpha)\cos\theta\sin\theta \\ (\beta-\alpha)\cos\theta\sin\theta & \alpha\sin^2\theta + \beta\cos^2\theta \end{pmatrix}. \tag{S9}$$

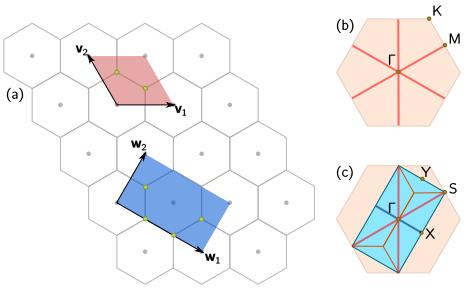

Supplementary Figure 3. (a) Primitive unit cell with two atoms (top), and rectangular supercell with four atoms (bottom) used when applying strain in a given direction β. In particular, $\mathbf{w}_1$ ($\mathbf{w}_2$) is along an armchair (zigzag) direction. Both $\mathbf{v}_1$ and $\mathbf{v}_2$ are along zigzag directions, instead. (b) Brillouin zone of the primitive unit cell. The six equivalent Γ−M lines are highlighted in red. (c) Folding of the Brillouin zone when the 4-atom supercell is considered (light blue rotated rectangle), and labelling of the high-symmetry points. The six Γ−M lines of panel (b) split into four Γ−S lines (red) and two Γ−X lines (dark blue).

Choosing the reference frame in which $\mu^{\mathrm{cond},0}$ is diagonal, we have to sum the 6 bands, each rotated by $\frac{\pi}{3}$ with respect to the previous one, and therefore

$$(\mu_{\mathrm{T}}^{\mathrm{cond}})_{11} = \frac{\alpha}{6}\sum_{i=0}^{5}\cos^2\left(i\cdot\frac{\pi}{3}\right) + \frac{\beta}{6}\sum_{i=0}^{5}\sin^2\left(i\cdot\frac{\pi}{3}\right). \tag{S10}$$

Now $\sum_{i=0}^{5}\sin^2\left(i\cdot\frac{\pi}{3}\right) = 0+\frac{3}{4}+\frac{3}{4}+0+\frac{3}{4}+\frac{3}{4} = 3$ and $\sum_{i=0}^{5}\cos^2\left(i\cdot\frac{\pi}{3}\right) = \sum_{i=0}^{5}1-\sin^2\left(i\cdot\frac{\pi}{3}\right) = 6-3 = 3$, and therefore $(\mu_{\mathrm{T}}^{\mathrm{cond}})_{11} = (\mu_{\mathrm{T}}^{\mathrm{cond}})_{22} = \frac{\alpha+\beta}{2}$. Similarly, one can show that the off-diagonal contributions cancel in pairs, and therefore the total conduction mobility is a multiple of the identity, with value

$$\boxed{\mu_{\mathrm{T}}^{\mathrm{cond}} = \frac{e\hbar^3}{2k_{\mathrm{B}}Tm_{\mathrm{DOS}}^{\mathrm{c}}}\left(\frac{C_{\mathrm{armchair}}}{(E_{\mathrm{armchair}}^{\mathrm{cond}})^2 m_{\mathrm{L}}^{\mathrm{c}}} + \frac{C_{\mathrm{zigzag}}}{(E_{\mathrm{zigzag}}^{\mathrm{cond}})^2 m_{\mathrm{T}}^{\mathrm{c}}}\right).} \tag{S11}$$

The fact that the μ_{T} tensor is isotropic is expected, because the system has hexagonal symmetry. Note that averaging on all valleys is equivalent to averaging the tensor of a single valley in all directions, as it is the case also for cubic systems [56].

Supplementary Note 5: Relevant valence band edges

Without SOC, in the valence band we have instead two single valleys that are degenerate at Γ, but with different masses (and scattering times), that we can call light holes (LH) and heavy holes (HH). We assume that both bands are parabolic, and in this case the 2D density of states is a step function (where the step height, occurring at the band edge energy, is proportional to the 2D DOS effective mass). Then, the population n_i of a given band is simply

$$n_i = D\cdot m_{\mathrm{DOS}}^{i} \tag{S12}$$

where D is a constant that contains the energy difference between the chemical potential and the band edge. (We are assuming that this energy difference is the same for both bands, true if intraband scattering events can quickly equilibrate the bands so that they have the same chemical potential, and if we consider an unstrained system so that the two LH and HH bands are degenerate at their maximum).

Replacing this simple expression for n_i in Supplementary Equations (S3) and (S5), the mobility is:

$$\mu_{\beta}^{\mathrm{val}} = e\cdot\frac{\frac{Dm_{\mathrm{DOS}}^{\mathrm{LH}}\tau_{\beta}^{\mathrm{LH}}}{(m_{\mathrm{LH}}^{*})_{\beta}} + \frac{Dm_{\mathrm{DOS}}^{\mathrm{HH}}\tau_{\beta}^{\mathrm{HH}}}{(m_{\mathrm{HH}}^{*})_{\beta}}}{D(m_{\mathrm{DOS}}^{\mathrm{LH}}+m_{\mathrm{DOS}}^{\mathrm{HH}})} = e\cdot\frac{\frac{m_{\mathrm{DOS}}^{\mathrm{LH}}\tau_{\beta}^{\mathrm{LH}}}{(m_{\mathrm{LH}}^{*})_{\beta}} + \frac{m_{\mathrm{DOS}}^{\mathrm{HH}}\tau_{\beta}^{\mathrm{HH}}}{(m_{\mathrm{HH}}^{*})_{\beta}}}{m_{\mathrm{DOS}}^{\mathrm{v}}} \tag{S13}$$

where $m_{\mathrm{DOS}}^{\mathrm{v}}$ is the total DOS mass in the valence. Finally, we can prove that in the valence the mobility does not depend on the DOS mass of each of the two valleys, but only on the total DOS mass and on the effective masses in the transport direction. In fact, by simply replacing Supplementary Equation (S2), one finally obtains:

$$\boxed{\mu_{\beta}^{\mathrm{val}}[\text{without SOC}] = \frac{e\hbar^3 C_{\beta}}{k_{\mathrm{B}}T}\cdot\frac{\frac{1}{(E_{\beta}^{\mathrm{LH}})^2(m_{\mathrm{LH}}^{*})_{\beta}} + \frac{1}{(E_{\beta}^{\mathrm{HH}})^2(m_{\mathrm{HH}}^{*})_{\beta}}}{m_{\mathrm{DOS}}^{\mathrm{v}}}.} \tag{S14}$$

When we include spin-orbit effects, we need to consider only the topmost valence band (as already discussed), and since the band is isotropic, we can also set its mass $m_{\mathrm{v}}^{*} = m_{\mathrm{DOS}}^{\mathrm{v}}$. The formula then simplifies to:

$$\boxed{\mu_{\beta}^{\mathrm{val}}[\text{with SOC}] = \frac{e\hbar^3 C_{\beta}}{k_{\mathrm{B}}T}\cdot\frac{1}{(E_{\beta}^{\mathrm{LH}})^2(m_{\mathrm{v}}^{*})^2}.} \tag{S15}$$

Supplementary Note 6: Calculation of the deformation potential

The deformation potential is calculated using finite differences starting from band energies calculated with DFT of systems strained along the two relevant transport directions (zigzag and armchair). Considering a given band edge i (for instance the topmost valence band at Γ, or the conduction band along the Γ−M line in As and Sb), we can define $\Delta V_{\beta}^{i} = \varepsilon^{i}(\Delta l_{\beta}) - \varepsilon^{i}(\Delta l_{\beta}=0)$, where $\varepsilon^{i}(\Delta l_{\beta})$ is

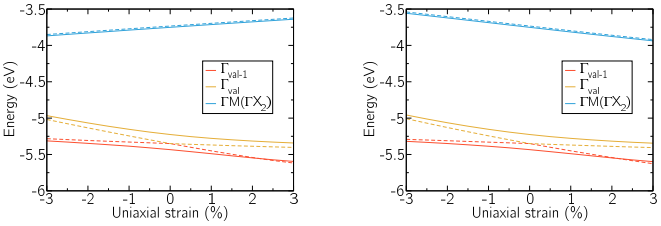

Supplementary Figure 4. Vacuum-level-corrected band edges as a function of the strain for the As monolayers. Left panel: strain along the $\mathbf{w}_1$ direction (armchair). Right panel: strain along the $\mathbf{w}_2$ direction (zigzag). Γ_{val} indicates the topmost valence band at Γ, $\Gamma_{\mathrm{val\text{-}1}}$ indicates the second valence band. Dashed curves refer to the case without SOC, while solid curves include SOC effects.

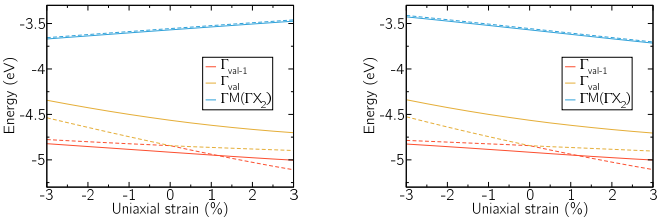

Supplementary Figure 5. Vacuum-level-corrected band edges as a function of the strain for the Sb monolayers. Left panel: strain along the $\mathbf{w}_1$ direction (armchair). Right panel: strain along the $\mathbf{w}_2$ direction (zigzag). Γ_{val} indicates the topmost valence band at Γ, $\Gamma_{\mathrm{val\text{-}1}}$ indicates the second valence band. Dashed curves refer to the case without SOC, while solid curves include SOC effects.

the energy of the $i-$th band edge for a system strained in the β direction by a quantity Δl_β. The deformation potential is then simply $E^i_\beta = \Delta V^i_\beta/(\Delta l_\beta/l_{\beta,0})$, where $l_{\beta,0}$ is the relaxed value of the lattice constant in the β direction, in the limit of small strains Δl_β. It is important to stress that the band-edge energies directly extracted from DFT calculations of different systems are ill-defined, because the position of the vacuum level can change in each calculation. We therefore use always vacuum-level-corrected band energies ε^i, obtained by defining, at each strain β, the vacuum level as the zero of energy. The vacuum level is obtained by calculating the averaged electrostatic potential in the region of space far away from the 2D layers. We verified that in all cases such potential is flat (within a 0.01 meV precision) $4-5$ Å away from the monolayers. We also note that the primitive 2D cell (with 2 atoms per cell) has non-orthogonal lattice vectors. In order to define strained systems in the two transport directions, we define a rectangular cell with 4 atoms per cell, where the two lattice vectors $\mathbf{w}_1$ and $\mathbf{w}_2$ are in the armchair and zigzag direction respectively, as shown in Supplementary Figure 3. Uniaxial strains are then applied to this rectangular supercell.

We consider 13 calculations for different, uniformly spaced strains between -3% and 3% for each of the two β directions, and we extract the deformation potential from the linear coefficient of a quadratic fit of the vacuum-level-corrected band edges, as shown in Supplementary Figs. 4 and 5, where we report results both with and without SOC.

Supplementary Note 7: Effective masses

We have computed the effective masses at zero strain in the primitive unit cell; we have checked that the effective masses do not change significantly with strain. The values (calculated as described below) are reported in Table 1 of the main paper when including SOC effects. We also report here, in Supplementary Table 3, the values calculated when SOC is not included.

Also in the case of effective masses, we have to distinguish two cases. In the conduction band, the masses can be calculated by a parabolic fit of the band energies along the two directions. We have used for the fit 21 $\mathbf{k}-$points around the band minimum (at zero strain) in the longitudinal and transverse directions. The DOS mass $m^{\rm c}_{\rm DOS}$ is instead obtained by a parabolic fit of the integrated DOS (to take into account non-parabolicity effects). The DOS has been calculated on a dense $\mathbf{k}-$mesh using Wannier interpolation. The conduction valleys are in a very good approximation parabolic and indeed $m^{\rm c}_{\rm DOS} \approx \sqrt{m^{\rm c}_{\rm L} m^{\rm c}_{\rm T}}$ (see Table 1 in the main paper).

In the valence band, without SOC and in the absence of strain we have two isotropic bands with two different masses, named heavy hole (HH) and light hole (LH) for the larger and smaller mass (in absolute value), respectively. A difficulty arises when we apply some strain: in this case, the two bands split and we need to know how to associate the lower-energy and higher-energy valence bands to corresponding effective mass (LH or HH). Actually, with strain the two masses become anisotropic tensors. In particular, given a direction β for the strain, we have checked that (both for As and Sb) the effective mass obtained fitting the bands for $\mathbf{k}-$points in the same direction as β is HH for the bands with larger deformation potential (smaller in absolute value, since $E<0$), while LH for the band with smaller deformation potential. Instead, if the $\mathbf{k}-$points are taken in a direction orthogonal to β, the two masses HH and LH are reversed. Since in Supplementary Equation (S14) we need only the deformation potential for strains along the same transport direction as the effective mass components, Supplementary Equation (S14) becomes:

$$\mu^{\rm val}_\beta = \frac{e\hbar^3 C_\beta}{k_{\rm B}T}\cdot\frac{\frac{1}{(E_\beta(v,i=1))^2(m^*_{\rm HH})_\beta}+\frac{1}{(E_\beta({\rm v},i=2))^2(m^*_{\rm LH})_\beta}}{m^{\rm v}_{\rm DOS}}, \tag{S16}$$

where we have defined $i=1,2$ consistently to Supplementary Table 1, i.e., so that $E_\beta({\rm v},i=2)<E_\beta({\rm v},i=1)$.

In the case with SOC, this difficulty does not arise because the two bands do not cross.

Supplementary Table 1. Deformation potentials (in eV) for the valence and conduction bands of As and Sb monolayers, both including and disregarding spin-orbit coupling effects. For valence bands with spin-orbit coupling, we only report the deformation potential of the topmost valence band; in the case without spin-orbit coupling, $i=1,2$ are defined so that $i=1$ is the topmost valence band for positive strain, and $i=2$ the second highest valence band for positive strain, equivalent to saying that we chose $i=1,2$ so that $E^{\rm val}_\beta(i=2)<E^{\rm val}_\beta(i=1)$. Results without spin-orbit coupling are consistent with previous calculations at the same level of theory [14].

With SOC	$E^{\rm val}_\beta$	$E^{\rm cond}_\beta(\Gamma-{\rm X})$
As (β = armchair)	-6.243	3.815
As (β = zigzag)	-6.386	-6.351
Sb (β = armchair)	-5.966	3.265
Sb (β = zigzag)	-6.078	-4.843

Without SOC	$E^{\rm val}_\beta(i=1)$	$E^{\rm val}_\beta(i=2)$	$E^{\rm cond}_\beta(\Gamma-{\rm X})$
As (β = armchair)	-1.997	-10.094	3.785
As (β = zigzag)	-1.922	-10.321	-6.380
Sb (β = armchair)	-2.006	-9.571	3.260
Sb (β = zigzag)	-1.969	-9.674	-4.895

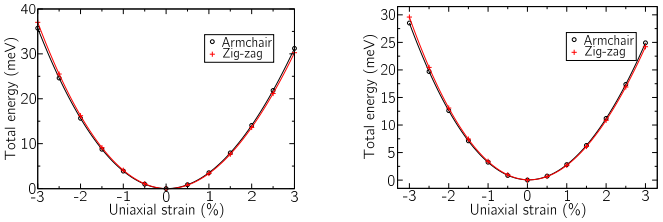

Supplementary Figure 6. Total energy as a function of the uniaxial strain (when SOC effects are not included) in the armchair (open points) and zigzag (plus symbols) direction. Left panel: As monolayer; right panel: Sb monolayer. The curves are the cubic fits of the data points used to obtain the elastic moduli.

Supplementary Table 2. 2D elastic moduli of the As and Sb monolayer systems, both including and disregarding spin-orbit coupling effects.

	S_0 (Å^2)	C_β (eV Å^{-2}) with SOC	C_β (eV Å^{-2}) without SOC
As (β = armchair)	22.5	3.271	3.299
As (β = zigzag)		3.279	3.308
Sb (β = armchair)	29.4	1.948	2.012
Sb (β = zigzag)		1.945	2.019

Supplementary Table 3. Effective masses of the relevant bands of arsenene and antimonene, in units of the electron mass m_0, when SOC is not included. Symbols are explained in the text. Note that $m^{\rm c}_{\rm DOS}$ is the effective DOS mass for each of the 6 identical conduction band valleys, while $m^{\rm v}_{\rm DOS}$ represents the total effective DOS mass for the two degenerate valence bands.

	As	Sb
$m^{\rm c}_{\rm DOS}$	0.273	0.260
$m^{\rm c}_{\rm L}$	0.508	0.461
$m^{\rm c}_{\rm T}$	0.150	0.149
$m^{\rm v}_{\rm DOS}$	0.554	0.523
$m^{\rm v}_{\rm HH}$	0.482	0.443
$m^{\rm v}_{\rm LH}$	0.077	0.073

Supplementary Table 4. Mobilities for arsenene and antimonene, estimated at $T = 300\,$K, in units of cm^{2}V^{-1}s^{-1}. Both the values obtained with and without spin-orbit coupling (SOC) are reported.

	With SOC		Without SOC	
	$\mu^{\rm val}$	$\mu^{\rm cond}$	$\mu^{\rm val}$	$\mu^{\rm cond}$
As	1700	635	1355	622
Sb	1737	630	946	641

Supplementary Note 8: Elastic moduli

The 2D elastic modulus in a given direction β is defined as:

$$C_\beta = \frac{1}{S_0}\,\frac{\partial^2 \mathcal{E}_{\Delta l_\beta}}{\partial(\Delta l_\beta/l_{\beta,0})^2}\bigg|_{\Delta l_\beta=0}, \qquad \text{(S17)}$$

where $\mathcal{E}_{\Delta l_\beta}$ is the total energy of a system strained uniaxially by $\Delta l_\beta/l_{\beta,0}$ in the β direction, and S_0 is the value of the unstrained unit-cell surface.

The values reported in the paper are obtained from the parabolic coefficient of a cubic fit of the total energy as a function of strain in the $[-3,+3]$% range for the four-atom supercells, shown in Supplementary Figure 6 for both materials (when SOC is included). In a hexagonal system the elastic tensor should be isotropic in the plane. Indeed, apart from numerical inaccuracies, the C_β values are the same for both directions (see Supplementary Table 2), and do not significantly change including or disregarding SOC.

Supplementary Note 9: Values of the mobility

Using the values of Supplementary Table 1, Table 1 (in the main paper) and Supplementary Table 2, calculated as described in the previous sections, we estimated the values for the mobilities at $T = 300\,$K, in units of cm^{2}V^{-1}s^{-1}, that we report in Supplementary Table 4. Note that since we expect that the total mobility is isotropic, we indicate only the average value obtained for the armchair and the zigzag directions. In any case, the values in the two directions differ (due to numerical errors) by less than 5%.

For completeness, we also report the value of the single-valley conduction mobility tensor, including spin-orbit coupling effects, in a basis set where the first vector is along the armchair direction and the second along the zigzag one, and expressed in units of cm^{2}V^{-1}s^{-1}:

$$\mu^{{\rm cond},i}_{\rm As} = \begin{pmatrix} 567 & 0 \\ 0 & 704 \end{pmatrix}, \qquad \mu^{{\rm cond},i}_{\rm Sb} = \begin{pmatrix} 507 & 0 \\ 0 & 753 \end{pmatrix}. \qquad \text{(S18)}$$

Using the formulas above, one can also calculate the scattering times of electrons with LA phonons, that turn out to be (in conduction): $\tau^{\rm As}_{\rm armchair} = 161\,$fs, $\tau^{\rm As}_{\rm zigzag} = 58\,$fs, $\tau^{\rm Sb}_{\rm armchair} = 136\,$fs, $\tau^{\rm Sb}_{\rm zigzag} = 62\,$fs. Finally, in order to estimate the mean free path, it is useful to evaluate the Fermi velocity for electrons in the $\Gamma-$M valleys, that for electrons along the i principal direction of the valley is given by:

$$v^{\rm F}_i = \sqrt{\frac{2\pi\hbar^2 n_{\rm dop}}{m_i m_{\rm DOS}}}, \qquad \text{(S19)}$$

where we have used the 2D DOS to relate the the effective doping of the system $n_{\rm dop}$ to the Fermi energy, and where m_i indicates the effective mass in the i direction. As a reference value, for a doping of $n_{\rm DOP} = 5\cdot 10^{13}\,$cm^{-2}, we obtain for As: $v^{\rm F}_{\rm L} = 0.55\,$nm fs^{-1}, $v^{\rm F}_{\rm T} = 1.01\,$nm fs^{-1}, while for Sb: $v^{\rm F}_{\rm L} = 0.60\,$nm fs^{-1}, $v^{\rm F}_{\rm T} = 1.04\,$nm fs^{-1}.

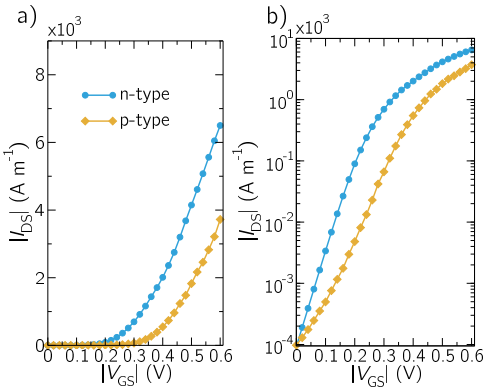

Supplementary Figure 7. $|I_{\rm DS}| - |V_{\rm GS}|$ curve in (a) linear and (b) semi-logarithmic scale for As n-MOS and p-MOS transistors and a gate length of $L_{\rm G}$=7 nm. Sb FETs show a similar behaviour and are not shown here.

Supplementary Note 10: n-MOS and p-MOS Field Effect Transistors

In order to span the whole device parameter space and optimise the device performances, we compare the $I-V$ curves of n-MOS and p-MOS devices in Supplementary Figure 7, in the case of a As device with $L_{\rm G}$ = 7 nm (similar results are obtained for Sb FETs).

As it can be seen, the n-MOS device shows larger currents and better SS as compared to the p-type device. For this reason, in the main text we decided to focus on n-MOSFETs only, in order to obtain the best performance against Industry requirements.

[1] Dresselhaus, M. S. A revolution of nanoscale dimensions. *Nat. Rev. Mat.* **1**, 15017 (2016).

[2] Novoselov, K. S. *et al.* Electric field effect in atomically thin carbon films. *Science* **306**, 666–669 (2004).

[3] Novoselov, K. S. *et al.* Two-dimensional gas of massless dirac fermions in graphene. *Nature* **438**, 197–200 (2005).

[4] Mak, K. F., Lee, C., Hone, J., Shan, J. & Heinz, T. F. Atomically Thin MoS_2: A New Direct-Gap Semiconductor. *Phys. Rev. Lett.* **105**, 136805 (2010).

[5] Radisavljevic, B., Radenovic, A., Brivio, J., Giacometti, V. & Kis, A. Single-layer MoS_2 transistors. *Nat. Nano.* **6**, 147–150 (2011).

[6] Tan, C. & Zhang, H. Two-dimensional transition metal dichalcogenide nanosheet-based composites. *Chem. Soc. Rev.* **44**, 2713–2731 (2015).

[7] Li, L. *et al.* Black phosphorus field-effect transistors. *Nat. Nano.* **9**, 372–377 (2014).

[8] Liu, H. *et al.* Phosphorene: An Unexplored 2D Semiconductor with a High Hole Mobility. *ACS Nano* **8**, 4033–4041 (2014).

[9] Qiao, J., Kong, X., Hu, Z.-X., Yang, F. & Ji, W. High-mobility transport anisotropy and linear dichroism in few-layer black phosphorus. *Nat. Commun.* **5**, 4475 (2014).

[10] Wang, H. *et al.* Black phosphorus radio-frequency transistors. *Nano Letters* **14**, 6424–6429 (2014).

[11] Du, Y., Liu, H., Deng, Y. & Ye, P. D. Device perspective for black phosphorus field-effect transistors: Contact resistance, ambipolar behavior, and scaling. *ACS Nano* **8**, 10035–10042 (2014).

[12] Avsar, A. *et al.* Air-stable transport in graphene-contacted, fully encapsulated ultrathin black phosphorus-based field-effect transistors. *ACS Nano* **9**, 4138–4145 (2015).

[13] Kamal, C. & Ezawa, M. Arsenene: Two-dimensional buckled and puckered honeycomb arsenic systems. *Phys. Rev. B* **91**, 085423 (2015).

[14] Wang, G., Pandey, R. & Karna, S. P. Atomically Thin Group V Elemental Films: Theoretical Investigations of Antimonene Allotropes. *ACS Appl. Mater. Interfaces* **7**, 11490–11496 (2015).

[15] Zhang, S., Yan, Z., Li, Y., Chen, Z. & Zeng, H. Atomically thin arsenene and antimonene: Semimetal–semiconductor and indirect–direct band-gap transitions. *Angew. Chem. Int. Ed.* **54**, 3112–3115 (2015).

[16] Zhu, Z., Guan, J. & Tománek, D. Strain-induced metal-semiconductor transition in monolayers and bilayers of gray arsenic: A computational study. *Phys. Rev. B* **91**, 161404 (2015).

[17] Lei, T. *et al.* Electronic structure of antimonene grown on Sb_2Te_3 (111) and Bi_2Te_3 substrates. *J. Appl. Phys.* **119**, 015302 (2016).

[18] NanoTCAD ViDES (2015). URL http://vides.nanotcad.com.

[19] Fiori, G. & Iannaccone, G. Multiscale modeling for graphene-based nanoscale transistors. *Proc. IEEE* **101**, 1653–1669 (2013).

[20] Porezag, D., Frauenheim, T., Köhler, T., Seifert, G. & Kaschner, R. Construction of tight-binding-like potentials on the basis of density-functional theory: Application to carbon. *Phys. Rev. B* **51**, 12947–12957 (1995).

[21] Tan, Y. *et al.* Empirical tight binding parameters for GaAs and MgO with explicit basis through DFT mapping. *J. Comp. Electron.* **12**, 56–60 (2013).

[22] Marzari, N., Mostofi, A. A., Yates, J. R., Souza, I. & Vanderbilt, D. Maximally localized Wannier functions: Theory and applications. *Rev. Mod. Phys.* **84**, 1419–1475 (2012).

[23] Lee, Y.-S., Nardelli, M. B. & Marzari, N. Band Structure and Quantum Conductance of Nanostructures from Maximally Localized Wannier Functions: The Case of Functionalized Carbon Nanotubes. *Phys. Rev. Lett.* **95**, 076804 (2005).

[24] Bruzzone, S., Iannaccone, G., Marzari, N. & Fiori, G. An open-source multiscale framework for the simulation of nanoscale devices. *IEEE Trans. Electron Devices* **61**, 48–53 (2014).

[25] Datta, S. *Electronic Transport in Mesoscopic Systems*, 1st edn. (Cambridge University Press, 1995).

[26] The International Techonology Roadmap for Semiconductors (2011). URL http://www.itrs2.net.

[27] Giannozzi, P. *et al.* QUANTUM ESPRESSO: a modular and open-source software project for quantum simulations of materials. *J. Phys. Condens. Matter* **21**, 395502 (2009).

[28] Pizzi, G., Cepellotti, A., Sabatini, R., Marzari, N. & Kozinsky, B. AiiDA: automated interactive infrastructure and database for computational science. *Comp. Mat.*

Sci. **111**, 218–230 (2016).

[29] Aufray, B. *et al.* Graphene-like silicon nanoribbons on Ag(110): A possible formation of silicene. *Appl. Phys. Lett.* **96**, 183102 (2010).

[30] Dávila, M. E., Xian, L., Cahangirov, S., Rubio, A. & Le Lay, G. Germanene: a novel two-dimensional germanium allotrope akin to graphene and silicene. *New J. Phys.* **16**, 095002 (2014).

[31] Fischetti, M. V. & Vandenberghe, W. G. Mermin-wagner theorem, flexural modes, and degraded carrier mobility in two-dimensional crystals with broken horizontal mirror symmetry. *Phys. Rev. B* **93**, 155413 (2016).

[32] Gunst, T., Markussen, T., Stokbro, K. & Brandbyge, M. First-principles method for electron-phonon coupling and electron mobility: Applications to two-dimensional materials. *Phys. Rev. B* **93**, 035414 (2016).

[33] Slotman, G. J., de Wijs, G. A., Fasolino, A. & Katsnelson, M. I. Phonons and electron-phonon coupling in graphene-h-BN heterostructures. *Annalen Der Physik* **526**, 381–386 (2014).

[34] Savrasov, S. Y., Savrasov, D. Y. & Andersen, O. K. Linear-response calculations of electron-phonon interactions. *Phys. Rev. Lett.* **72**, 372–375 (1994).

[35] Giustino, F., Cohen, M. L. & Louie, S. G. Electron-phonon interaction using Wannier functions. *Phys. Rev. B* **76**, 165108 (2007).

[36] Bardeen, J. & Shockley, W. Deformation potentials and mobilities in non-polar crystals. *Phys. Rev.* **80**, 72–80 (1950).

[37] Takagi, S., Toriumi, A., Iwase, M. & Tango, H. On the universality of inversion layer mobility in Si MOSFET's: Part II-effects of surface orientation. *IEEE Trans. Electron Devices* **41**, 2363–2368 (1994).

[38] Xi, J., Long, M., Tang, L., Wang, D. & Shuai, Z. First-principles prediction of charge mobility in carbon and organic nanomaterials. *Nanoscale* **4**, 4348–4369 (2012).

[39] Liao, B., Zhou, J., Qiu, B., Dresselhaus, M. S. & Chen, G. Ab initio study of electron-phonon interaction in phosphorene. *Phys. Rev. B* **91**, 235419 (2015).

[40] Cai, Y., Zhang, G. & Zhang, Y.-W. Polarity-Reversed Robust Carrier Mobility in Monolayer MoS_2 Nanoribbons. *J. Am. Chem. Soc.* **136**, 6269–6275 (2014).

[41] Radisavljevic, B. & Kis, A. Reply to 'Measurement of mobility in dual-gated MoS_2 transistors'. *Nat. Nano.* **8**, 147–148 (2013).

[42] Moore, G. Cramming more components onto integrated circuits. *Electron. Mag.* **38**, 114–117 (1965).

[43] Taur, Y. & H., N. T. *Fundamentals of modern VLSI devices*, 1st edn. (Cambridge University Press, 2001).

[44] Lam, K. T., Dong, Z. & Guo, J. Performance limits projection of black phosphorous field-effect transistors. *IEEE Electron Device Letters* **35**, 963–965 (2014).

[45] Liu, F., Wang, Y., Liu, X., Wang, J. & Guo, H. Ballistic transport in monolayer black phosphorus transistors. *IEEE Trans. Electron Devices* **61**, 3871–3876 (2014).

[46] Perdew, J. P., Burke, K. & Ernzerhof, M. Generalized gradient approximation made simple. *Phys. Rev. Lett.* **77**, 3865–3868 (1996).

[47] Standard Solid State Pseudopotentials (SSSP) (2015). URL http://www.materialscloud.org/sssp.

[48] Vanderbilt, D. Soft self-consistent pseudopotentials in a generalized eigenvalue formalism. *Phys. Rev. B* **41**, 7892–7895 (1990).

[49] Dal Corso, A. Pseudopotentials periodic table: From H to Pu. *Comp. Mat. Sci.* **95**, 337–350 (2014).

[50] Garrity, K. F., Bennett, J. W., Rabe, K. M. & Vanderbilt, D. Pseudopotentials for high-throughput DFT calculations. *Comp. Mat. Sci.* **81**, 446–452 (2014).

[51] Pseudo Dojo (2016). URL http://www.pseudo-dojo.org.

[52] Marzari, N. & Vanderbilt, D. Maximally localized generalized Wannier functions for composite energy bands. *Phys. Rev. B* **56**, 12847–12865 (1997).

[53] Souza, I., Marzari, N. & Vanderbilt, D. Maximally localized Wannier functions for entangled energy bands. *Phys. Rev. B* **65**, 035109 (2001).

[54] Mostofi, A. A. *et al.* wannier90: A tool for obtaining maximally-localised Wannier functions. *Comp. Phys. Comm.* **178**, 685–699 (2008).

[55] Mostofi, A. A. *et al.* An updated version of wannier90: A tool for obtaining maximally-localised Wannier functions. *Comp. Phys. Comm.* **185**, 2309–2310 (2014).

[56] Herring, C. & Vogt, E. Transport and deformation-potential theory for many-valley semiconductors with anisotropic scattering. *Phys. Rev.* **101**, 944–961 (1956).